Hindawi
Mobile Information Systems
Volume 2022, Article ID 1810862, 10 pages
https://doi.org/10.1155/2022/1810862

Research Article

Lightning the Electromagnetic Pulse Coupling of Airborne Secondary Radar Electronic Equipment Using Intelligent Computing

Zhongyi Zhao and Shenyu Wang

Faculty of Mechanical Engineering and Automation, Liaoning University of Technology, Jinzhou 121001, Liaoning, China

Correspondence should be addressed to Zhongyi Zhao; jxzhaozy@lnut.edu.cn

Received 25 April 2022; Revised 30 May 2022; Accepted 29 June 2022; Published 30 July 2022

Academic Editor: Mian Ahmad Jan

In order to analyze the lightning coupling of the airborne secondary radar electronic equipment, this study analyzes the transient electromagnetic field strength of the airborne secondary radar electronic equipment and the current density distribution on the aircraft surface when the lightning directly hits the aircraft based on the simulation technology of the transmission-line matrix method. On this basis, the simulation research of field distribution and cable coupling is further carried out. Through the simulation calculation, it can be seen that when the lightning strikes the aircraft, the current density is relatively small in the continuous parts of the upper and lower surfaces of the fuselage and the middle of the wing. In addition to the areas where the lightning current is easily attached, structural irregularities such as windows, engines, front and rear edges of wings, and outboard antennas are often affected by edge effects, and the current density is often concentrated, requiring key protection. For more sensitive electronic equipment, the cable connected to it can be considered to use an appropriate type of shielded cable to achieve the shielding effect on the electromagnetic environment.

1. Introduction

The effects of lightning on the aircraft and the effects reproduced in experiments by simulating the lightning waveform can be divided into direct effects and indirect effects.

In some cases, the same aircraft components may have both direct and indirect effects [1, 2]. For example, lightning strikes and damages the antenna, while transmitting harmful voltages generated by electromagnetic energy to the transmitter or receiver connected to the antenna [3, 4]. In this case, physical damage to the antenna can be seen as a direct effect. The voltage or current or both voltage and current connected by the antenna to the radio or radar equipment are considered as indirect effects.

When lightning attaches to the nose of an aircraft (on the radome) or discharges in its vicinity, the transient process of the lightning current generates a powerful electromagnetic field of lightning pulses. Under the effect of electromagnetic coupling, part of the lightning energy will be conducted or radiated to the onboard electronic and electrical equipment in the front cabin. This will lead to the failure of the aircraft's central control computer, display console, fuel instrument, radar, and other equipment that endanger flight safety, resulting in catastrophic aircraft accidents [5, 6]. The goal of aircraft lightning indirect effect protection is to reduce the internal lightning transient environment of the electrical and electronic systems in the aircraft and their interconnecting harness areas. In this way, the actual transient level coupled at the equipment interface through the interconnection harness is not greater than the expected transient control level [7]. To this end, we conduct lightning coupling analysis and simulation research on airborne secondary radar electronic equipment.

2. Research on Simulation Methods

Due to the high cost and high cost of conducting the whole machine test, it is difficult to organize and coordinate, and it is difficult to obtain more comprehensive data at one time

[8, 9]. Therefore, as a numerical simulation technology, it plays an increasingly important role in the electromagnetic accurate calculation of the whole machine and equipment. To this end, we apply electromagnetic simulation tools to predict the lightning coupling of the airborne secondary radar electronics when lightning strikes the aircraft. The numerical simulation scheme is mainly designed according to the definition of current waveform in SAE-ARP5412 and SAE-ARP5416 and the test method of lightning protection [10, 11].

In the test method of SAE-ARP5416 lightning protection, the injection method of high-current pulse waveform is used to simulate lightning hitting the aircraft [12, 13]. Therefore, to analyze the electromagnetic phenomena caused by the indirect effect of lightning, it is necessary to first establish simulation models such as the discharge channel, the entry/exit point of the lightning current on the aircraft, the airborne secondary radar electronic equipment, and the wiring of the cable harness. The current source mainly adopts the current waveform A [14, 15] defined in SAE-ARP5412.

After the model is established, two aspects are mainly considered in the simulation stage of the indirect effect of aircraft lightning [16]as follows:

(1) We analyze the transient electromagnetic field distribution and current density distribution in the vicinity of the airborne secondary radar electronic equipment in the aircraft due to the direct lightning strike on the aircraft.

(2) We analyze the induced current at the load of the cable connected to the airborne secondary radar electronic equipment.

The transmission-line matrix method [17] was chosen for the simulation. This method can calculate the current density and field distribution on the inner and outer surfaces of the aircraft, and the induced current on the load of the cable port.

The steps of the electromagnetic environment simulation study of the location of the electronic equipment in the airborne secondary radar cabin mainly include the following steps [18]:

(1) We select electromagnetic calculation software and calculation method.

(2) We establish a simulation environment.

(3) We determine the model simulation parameters.

(4) We extract and analyze simulation results.

The establishment of the simulation environment mainly includes the selection of simulation software, the application of simulation methods, the establishment of simulation models, and the optimization of simulation models. Establishing a reasonable simulation environment is the foundation of the follow-up research, and it is also the guarantee of the correct research results.

3. The Establishment of the Numerical Simulation Model

3.1. The Establishment of Simulation Model. In this study, the IL-76 aircraft is used as the simulation object, and the coupled analysis of the lightning indirect effect of the airborne secondary radar electronic equipment is carried out. The installation position of the secondary radar antenna and its transponder on the aircraft is shown in Figure 1.

The simulation considers that the lightning current flows in from the nose of the machine and flows out from the vertical tail of the machine. We observe the field distribution near the airborne secondary radar equipment and the induced current and induced voltage on the cable load, which is shown in Figure 2.

Since the windows of the cargo hold section of the transport aircraft are small, but the opening of the tail hatch is large, the most unfavorable effect is considered in the simulation, that is, there is a certain gap at the tail hatch [19]. Since the electronic equipment of the airborne secondary radar is partly located at the vertical tail, it is convenient to set the gap to analyze the influence of the lightning current on the electronic equipment when it flows through the airframe, namely, the following:

(1) From the lower part of the fuselage to the mid-back edge of the upper part of the fuselage.

(2) From the upper middle rear edge of the aircraft fuselage to the aircraft tail.

The lightning electromagnetic pulse will affect the cables connected to the airborne secondary radar electronic equipment. For this reason, we focus on the induced current and induced voltage of the connecting cables of the secondary equipment [20]. For the study, two cables were laid inside the aircraft.

The two cables are separated by a distance at the upper middle rear edge of the aircraft fuselage. In order to facilitate the division and calculation of the grid, the cables are in vertical contact with the fuselage during wiring, and the distance from the fuselage is greater than one grid length. In order to improve the calculation accuracy, a refined mesh can be performed at the location where the secondary electronic equipment is located.

3.2. Setting of Simulation Parameters. In the scheme, the first strike back current component A is used for simulation, and this waveform is determined by the important parameters of the positive and negative first strike back [21, 22]. In the model, the biexponential current waveform is injected at the nose of the aircraft, and the outflow point is set at the tail of the aircraft and connected with the absorption boundary to be output as a loop.

Since 95% of the lightning current energy is concentrated in the 1 MHz frequency range, the highest frequency does not exceed several tens of MHz, so the frequency range is even 0~30 MHz in the simulation.

The frequency and time step settings are shown in Figure 3.

The fuselage material is set to metal aluminum; the fairing and tail are set to composite materials with a conductivity of 6.4; and the background computational domain is set to vacuum.

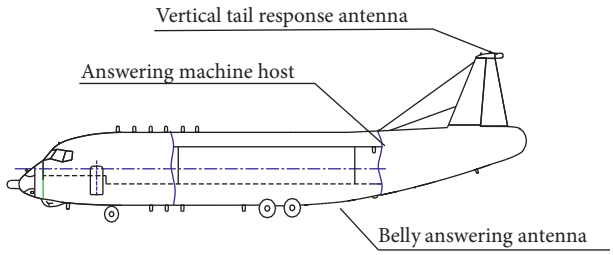

Figure 1: Schematic diagram of the installation location of radar electronic equipment.

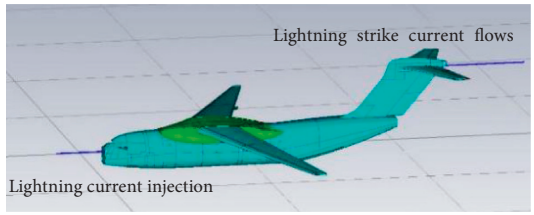

Figure 2: Schematic diagram of lightning current injection.

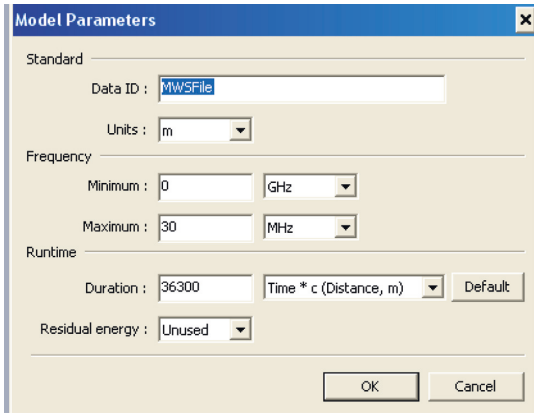

Figure 3: Frequency and time step settings.

In order to simulate the process of electromagnetic waves propagating in space, each surface of the computational domain is set as the absorption boundary condition; the reflection effect of the radiation field at the absorption boundary is reduced; and the computational domain is expanded to 10% of the grid. Since the lightning channel needs to form a current loop, the two surfaces in the x direction are directly connected to the injection point and the outflow point of the lightning current, that is, the expanded grid is 0, which are shown in Figure 4.

After several simulations with different conditions and parameters, the results show that when the number of grids is controlled at 3.682 M, the calculation accuracy can be guaranteed, and the calculation time can be controlled within a reasonable range. The specific settings are shown in Figure 5.

In order to focus on analyzing the electromagnetic field strength and field strength distribution in the area where the airborne secondary radar electronic equipment is located, a number of electromagnetic field probes are set up in

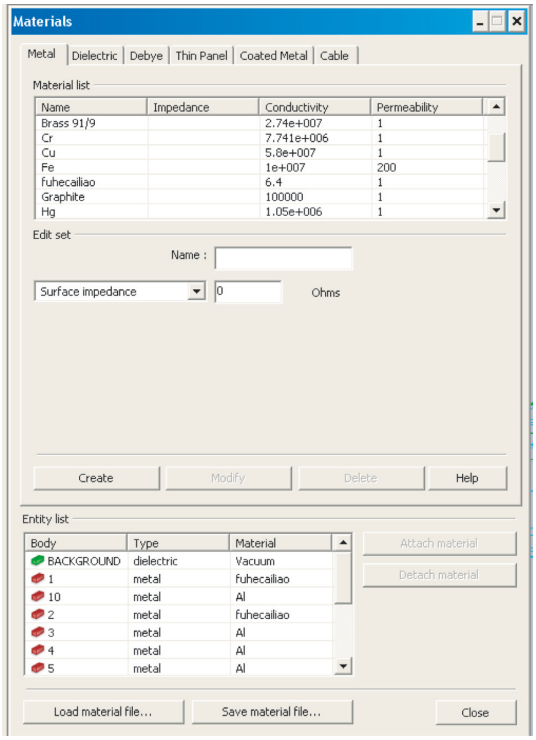

Figure 4: Airframe material settings.

different areas such as the belly, tail, and vertical tail of the aircraft.

Although the duration of the lightning current A wave waveform is 500 μs, its rising edge is 6.4 μs, and the half-width is 79 μs. In order to reduce the calculation time, we focus on the change in the electromagnetic field during the 100 μs process. The specific settings are shown in Figure 6.

Since the main energy of the lightning current is concentrated in the low frequency, we focus on the electromagnetic field distribution of 10 KHz. The output results include electric field, magnetic field, surface current, etc. The condition parameters are shown in Figure 7.

3.3. Surface Current Distribution of the Whole Machine during Lightning Strike. Figure 8 shows the color difference diagram of the surface current distribution of the whole machine at 5 μs.

Figures 9 and 10 show the electromagnetic field distribution in the whole aircraft space when lightning strikes the aircraft. It can be seen that the current density is relatively small at the continuation of structures such as the upper and lower surfaces of the fuselage and the middle of the wing. In addition to the areas where the lightning current is easily attached, structural irregularities such as windows, engines, and front and rear edges of wings are often affected by edge effects, and the current density is also relatively concentrated, which also requires key protection.

3.4. Electromagnetic Field Coupling Analysis at the Tail. Some of the airborne radar's electronics are located at the tail fairing of the aircraft. Therefore, the intensity and

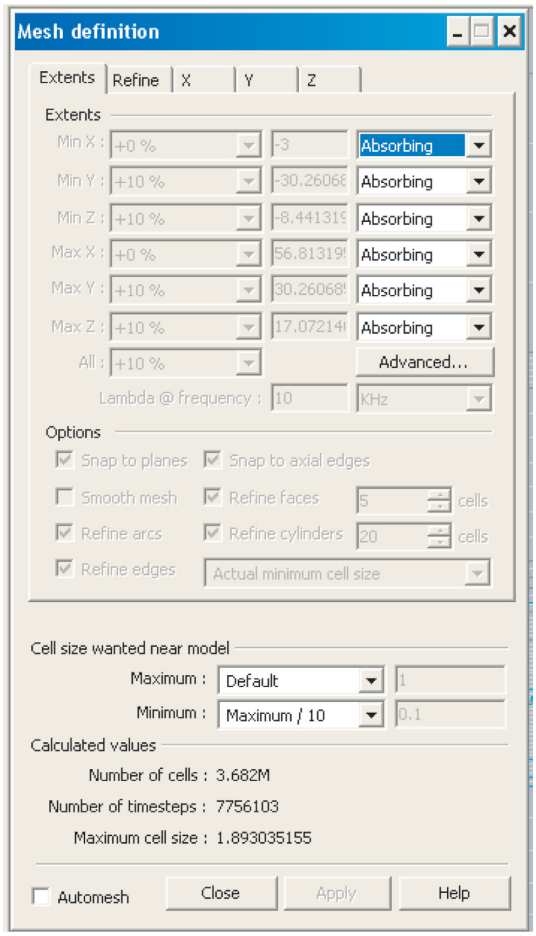

Figure 5: Setting of absorbing boundary conditions.

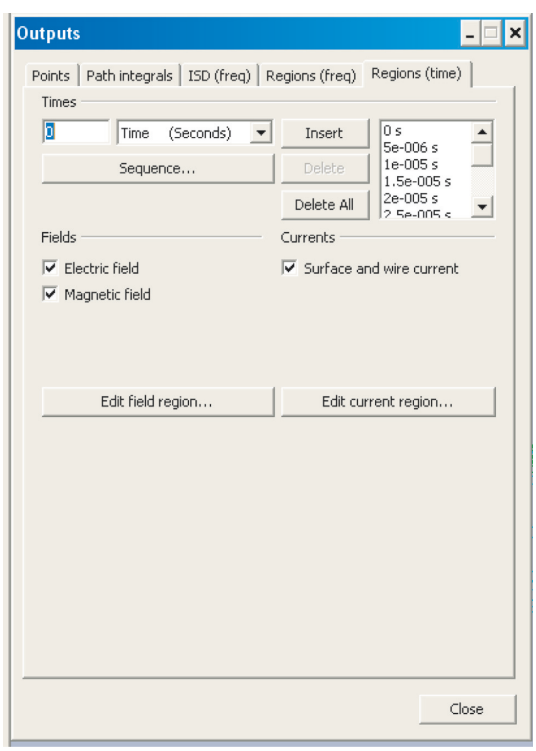

Figure 6: Time-domain parameter settings.

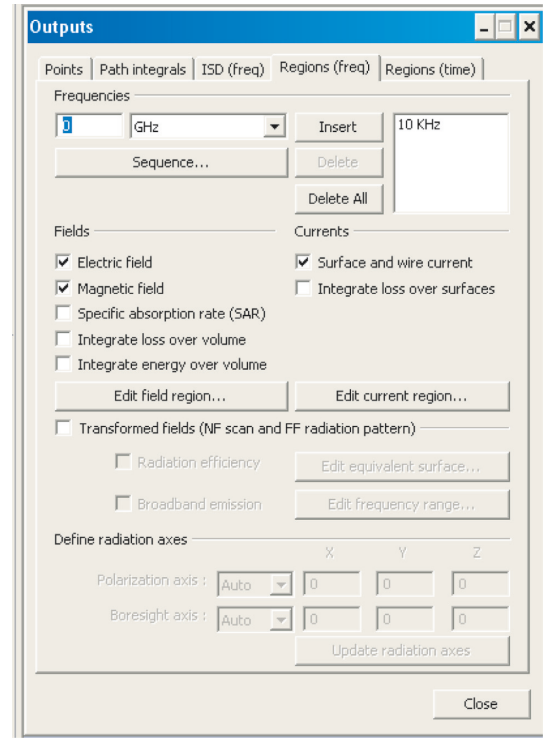

Figure 7: Frequency-domain field distribution parameter settings. IV simulation results and analyses.

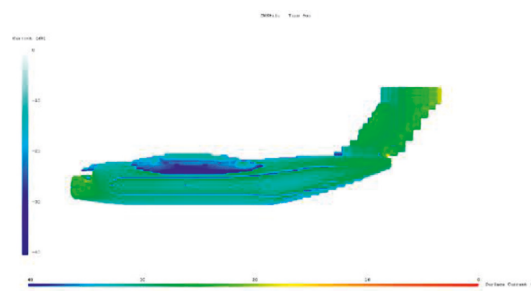

Figure 8: Transient surface current distribution of aircraft at 5 μs.

distribution of the electromagnetic field at different positions in the aircraft tail fairing are mainly analyzed. The key test locations are shown in Figure 11.

Figure 12 shows the time-domain waveform of the electric field at the tail. It can be seen that when the $a1$ point is shifted to the right by 1 m along the x direction to take the $a2$ point, the field strength decreases, and the magnitude is large. When the $a1$ point is shifted to the left by 1 m along the x direction, and the $a3$ point is taken, the field strength decreases, and the decrease range is larger. When the point $a1$ is translated 1 m downward along the z direction, the point $a6$ is taken, and the field strength greatly decreases.

Figure 13 shows the time-domain waveforms of the magnetic field at different observation points at the tail. It can be seen from the analysis in the figure that when the $a1$ point is shifted to the right by 1 m along the x direction to take the $a2$ point, the field strength increases, and the amplitude is very large. When the $a1$ point is shifted to the

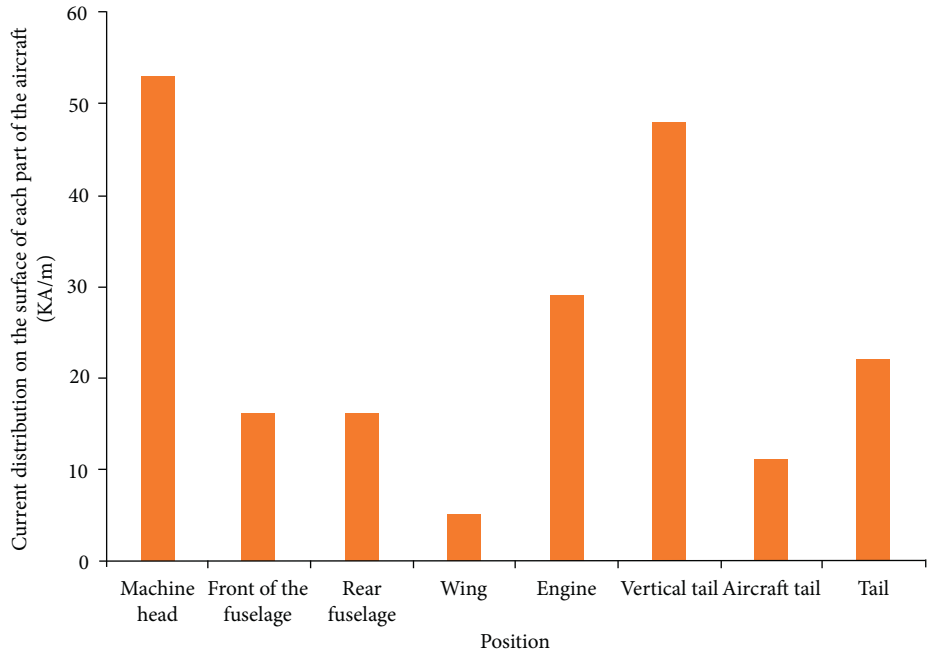

Figure 9: Surface current distribution of various parts of the aircraft.

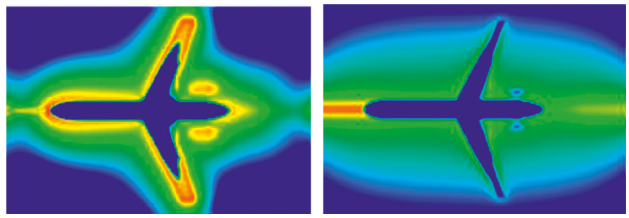

E *H*

Figure 10: Top view of electromagnetic field distribution in space.

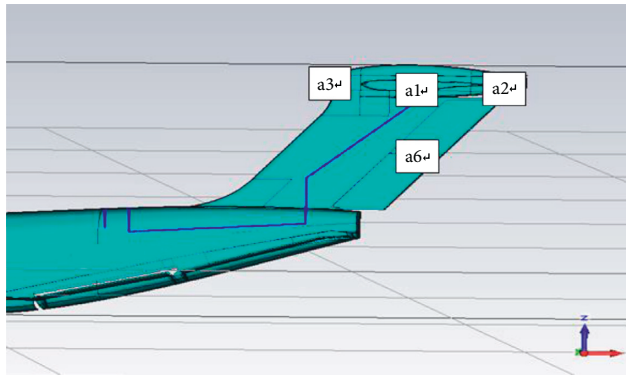

Figure 11: Distribution of detection points at the tail.

left by 1 m along the x direction, and the $a3$ point is taken, the field strength decreases, and the decrease is very large. When the point $a1$ is translated down 1 m along the z direction, the point $a6$ is taken, and the field strength decreases. The closer to the rear gap of the tail, the stronger the magnetic field. The farther away from the gap, the smaller the magnetic field strength. The strength of the magnetic field decreases as the height of the fuselage decreases.

3.5. Electromagnetic Field Coupling Analysis at the Rear of the Cargo Hold. The airborne secondary radar equipment transponder is located in the rear of the cargo compartment. Figure 14 shows the distribution of probe points at the transponder.

Through simulation calculation, Table 1 gives the peak value of electric field strength near the transponder.

When $b1$ translates 1 m to the right along the x direction, we take point $b4$ and find that the field strength becomes larger, but the magnitude is not large. When $b1$ translates 1 m to the right along the y direction, we take point $b2$ and find that the field strength becomes larger. When $b1$ translates 1 m to the left along the y direction, we take point $b3$ and find that the field strength increases. When $b1$ translates up 0.5 m along the z direction, taking point $b5$, it is found that the field strength becomes smaller. When $b1$ translates down 0.5 m along the z direction, taking point $b6$, it is found that the field strength increases. $b1$ takes point $c1$ to the left; $c1$ is translated to the left by 1 m to become $c4$; and the field strength becomes slightly larger.

$c1$ is shifted upward by 0.5 to become $c5$, and the field strength is slightly reduced. $c1$ drops by 0.5 to become $c6$, and the field strength is almost unchanged. When $c1$ is shifted to the right along the y direction by 1, it becomes $c2$, and the field strength significantly increases. $c1$ is shifted to the left along the y direction by 1 to become $c3$, and the field strength also significantly increases.

It can be concluded that the electric field strength increases from the transponder to both sides along the x direction. Decreasing the height of the point at the transponder also increases the electric field strength, because the lower point is closer to the landing gear, which is slotted into which the external electric field can leak.

Table 2 gives the peak value of the magnetic field strength in the vicinity of the transponder. It can be seen from the

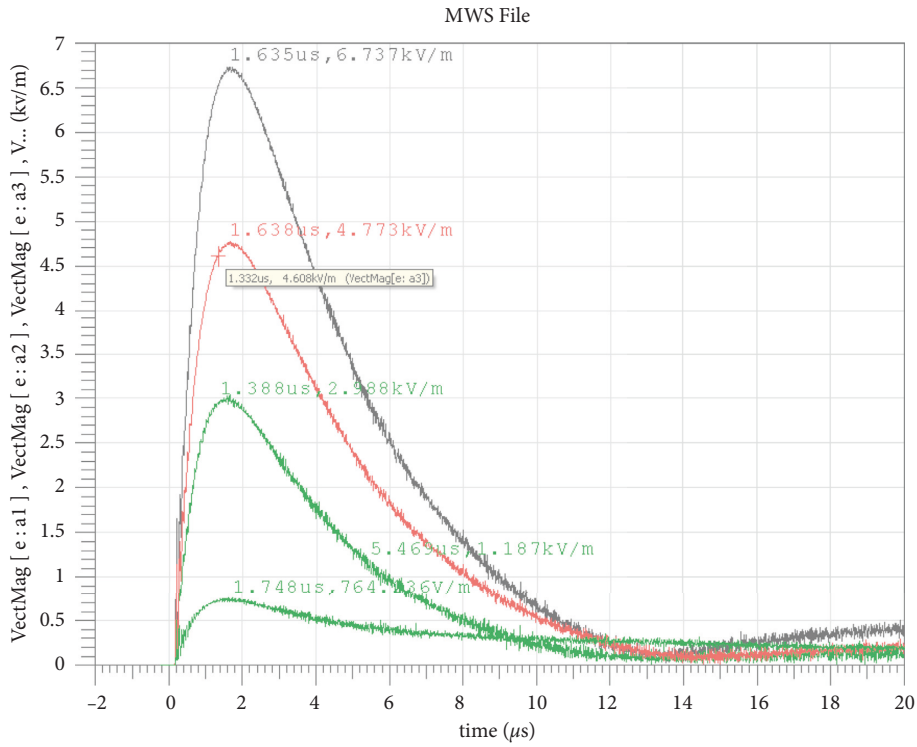

Figure 12: Time-domain waveform of electric field at tail.

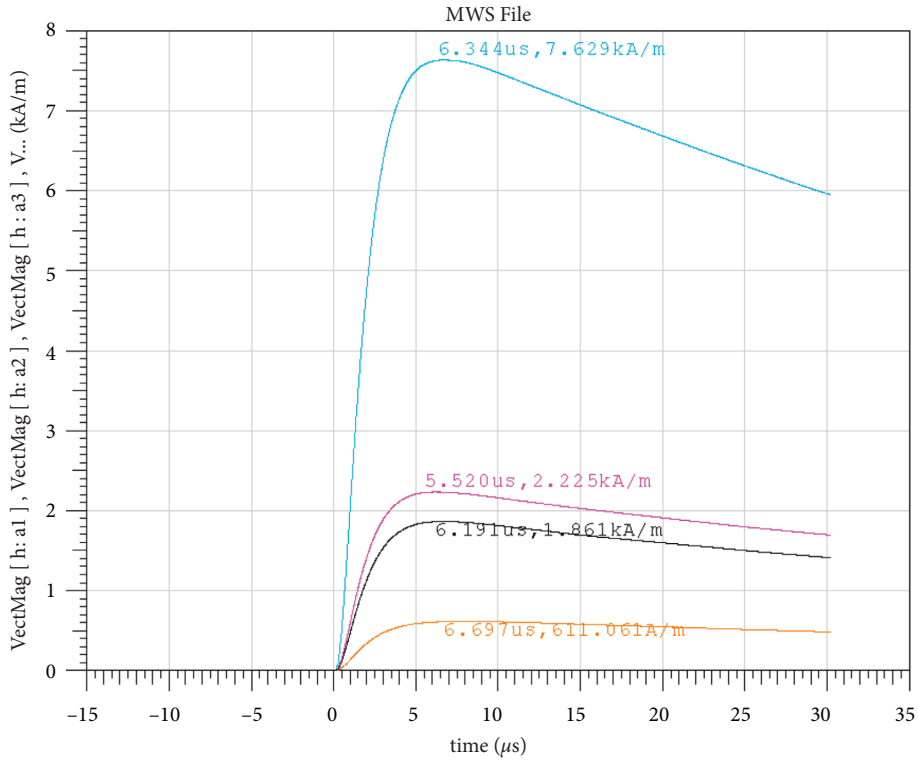

Figure 13: Magnetic field waveform at the tail.

analysis that $b1$ takes point $c1$ to the left, $c1$ is translated to the left by 1 m to become $c4$, and the magnetic field decreases; $c1$ is translated up by 0.5 to become $c5$, and the magnetic field decreases; $c1$ is translated downward by 0.5 to become $c6$, and the magnetic field is basically unchanged; $c1$ is shifted to the right by 1 along the y direction to become $c2$,

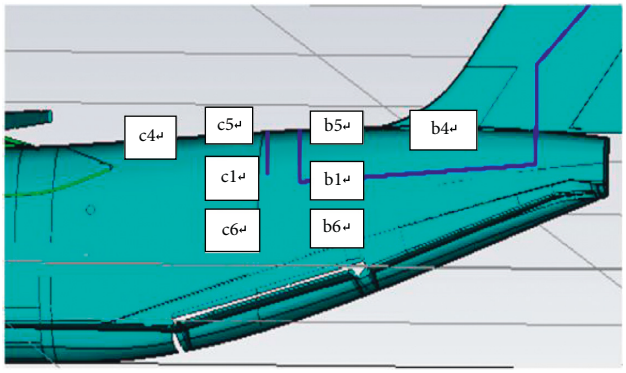

Figure 14: Distribution of detection points at the transponder.

Table 1: Peak value of electric field intensity near the transponder (V/m).

$B1$	$B2$	$B3$	$B4$	$B5$	$B6$
474.19	975.40	1207	602.08	313.81	562.36
$C1$	$C2$	$C3$	$C4$	$C5$	$C6$
508.87	895.41	878.13	598.49	315.97	488.72

Table 2: Peak value of magnetic field strength near the transponder (A/m).

$B1$	$B2$	$B3$	$B4$	$B5$	$B6$
28.232	25.450	27.993	35.969	24.869	34.462
$C1$	$C2$	$C3$	$C4$	$C5$	$C6$
22.842	21.445	24.706	12.539	18.875	29.287

and the magnetic field is basically unchanged; $c1$ is shifted to the left along the y direction by 1 to become $c3$, and the magnetic field is basically unchanged. That is, the closer the transponder is to the middle of the fuselage, the smaller the magnetic field strength, the lower the height, and the greater the magnetic field strength.

3.6. Coupling Analysis of Electromagnetic Field at the Belly. Figure 15 shows the distribution of observation points at the belly of the aircraft, and the electromagnetic field strength at each observation point is simulated and calculated.

Table 3 gives the peak value of the electric field strength at the belly. It can be seen that $d1$ moves to the right along the x direction by 1 m to become $d2$, and the field strength is found to be significantly reduced. $d1$ moves 1 m to the left along the x direction to become $d3$, and the field strength decreases. $d1$ moves 1 m to the right along the y direction to become $d4$, and the field strength significantly decreases. $d1$ moves 1 m to the left along the y direction to become $d5$, and the field strength also significantly increases. $d1$ goes up 0.5 in the z direction to become $d6$, and the field strength increases. $d1$ goes down 0.5 in the z direction to become $d7$, and the field strength slightly decreases. The point electric field intensity in the middle section of the belly is the largest, and the electric field intensity decreases toward both sides.

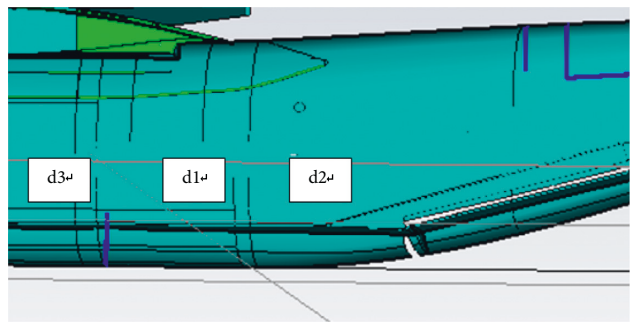

Figure 15: Distribution of detection points at the belly.

Table 3: Peak value of electric field intensity at the belly (V/m).

$D1$	$D2$	$D3$	$D4$	$D5$	$D6$	$D7$
2099	1040	1273	915.582	8309	2824	1641

Table 4 gives the peak value of the magnetic field strength at the belly. It can be seen that $d1$ moves to the right along the x direction by 1 m to become $d2$, and the field strength is found to be significantly reduced. $d1$ moves 1 m to the left along the x direction to become $d3$, and the field strength increases. $d1$ moves 1 m to the right along the y direction to become $d4$, and the field strength decreases. $d1$ moves 1 m to the left along the y direction to become $d5$, and the field strength also significantly increases. $d1$ goes up by 0.5 in the z direction to become $d6$, and the field strength increases. $d1$ goes down 0.5 in the z direction to become $d7$, and the field strength slightly decreases. The magnetic field strength at the belly decreases with the increase in the x coordinate, and the greater the height of the point at the belly, the greater the magnetic field strength.

3.7. Electromagnetic Field Distribution Near Airborne Secondary Radar Electronic Equipment. Airborne secondary radar electronic equipment is mainly concentrated near the tail and belly of the aircraft. The lightning electromagnetic pulse field caused by the lightning current will have a great impact on nearby equipment and cables.

Figure 16 to Figures 3, 5, and 9 are the electromagnetic field chromatic aberration distribution diagrams near the airborne secondary radar electronic equipment. Red areas represent larger field strengths, while blue areas represent smaller field strengths.

It can be seen from Figures 16 and 17 that the electric field strength in the center of the cabin near the transponder is the smallest. Due to the influence of the hatch, the closer to the sides, the greater the electric field strength, and the electric field in the lower part above the floor is slightly larger than that in the upper part. As for the magnetic field, also due to the leakage of the electromagnetic field from the hatch, the magnetic field strength of the upper part is obviously smaller than that of the lower part.

Figure 18 is the front view of the electromagnetic field distribution at the window. As can be seen from the figure, due to the leakage of the electromagnetic field at the window,

Table 4: Peak value of magnetic field strength at the belly (A/m).

*D*1	*D*2	*D*3	*D*4	*D*5	*D*6	*D*7
19.29	16.39	50.19	18.19	65.22	28.55	18.43

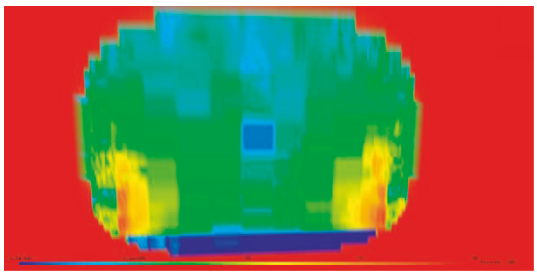

Figure 16: Front view of electric field distribution near the transponder.

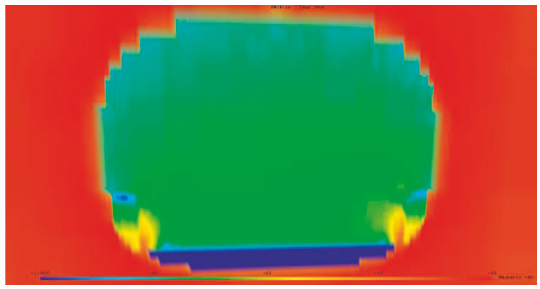

Figure 17: Front view of magnetic field distribution near the transponder.

the closer to the window, the greater the electric field strength. At the center of the nacelle, the electric field strength is the smallest.

It can be seen from Figures 19 and 20 that the electric field strength is the smallest at the fairing and the slit at the lower part of the fuselage. There can also be a part of the field strength in the middle of the fuselage that is very small; the field strength gradually increases from the middle of the fuselage to both sides; and the field strength is the largest at the tail. The magnetic field strength is the smallest at the front of the fuselage, gradually increases from the front to the middle and rear, and reaches the maximum at the tail.

It can be seen from Figures 21 and 22 that in the vicinity of the radome, the window, and the tail hatch, the electric field obviously changes due to the transmission and leakage of electromagnetic waves. The closer to the hole, the greater the electric field strength, and the smaller the field value at the center of the nacelle. For the magnetic field, the effect of holes is not obvious. Among them, from the rear of the fuselage to the front, the field strength gradually increases. The magnetic field in the middle of the fuselage is the smallest, and the magnetic field gradually increases toward the rear.

3.8. Cable Coupling Analysis of Electronic Equipment. Figure 23 is a diagram of the cable layout inside the fuselage. When the connecting cable of the airborne secondary radar

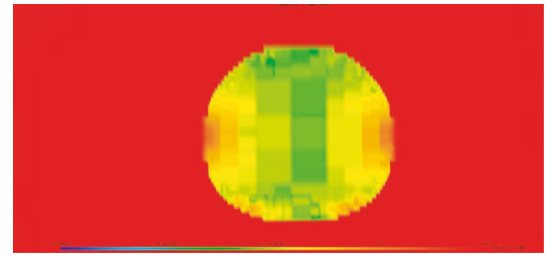

Figure 18: Front view of electric field distribution at the window.

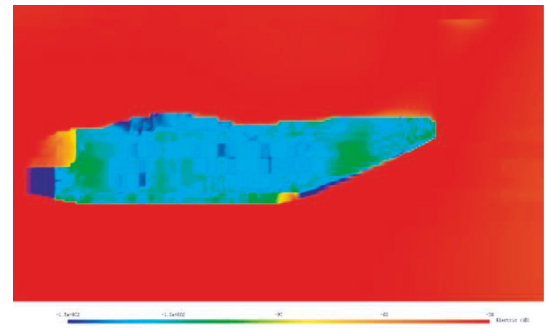

Figure 19: Side view of electric field distribution inside the cabin.

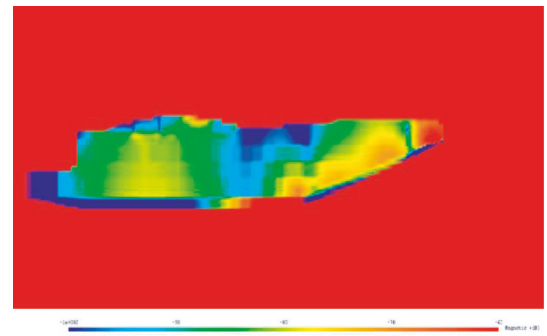

Figure 20: Side view of the magnetic field distribution inside the cabin.

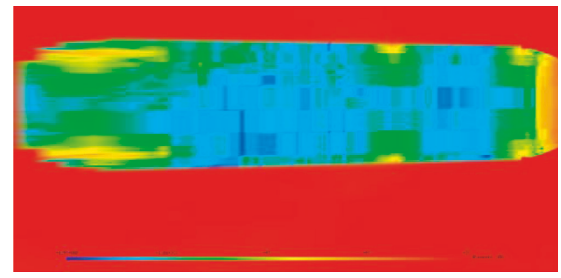

Figure 21: Top view of electric field distribution inside the cabin.

electronic equipment is a coaxial cable with a load of 50 ohms, the peak current and peak voltage values induced on it are shown in Table 5.

Because the current flows from the nose to the tail of the machine, the current of the internal cable near the nose is always greater than that far from the nose. The same goes for voltage. When the current decreases, due to the different

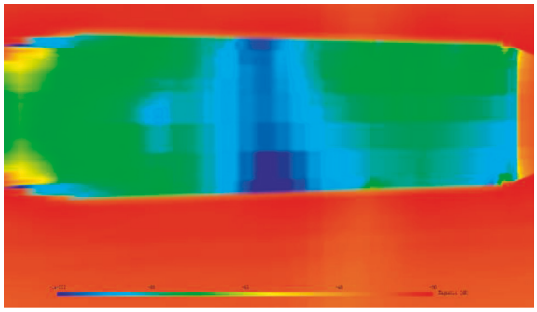

Figure 22: Top view of the magnetic field distribution inside the cabin.

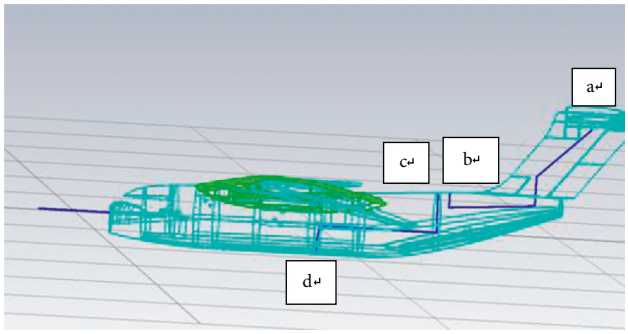

Figure 23: Cable arrangement inside the fuselage.

Table 5: Coupling current (A) and voltage (V) of the terminal on the coaxial 50 Ω cable.

Coupling current		Coupling voltage	
Ia	0.317	*Va*	15.862
Ib	2.036	*Vb*	101.784
Ic	5.012	*Vc*	250.594
Id	5.634	*Vd*	281.698

external magnetic fields in different regions, the coupling effect on the cable is also different.

In order to effectively reduce the weight of the aircraft, most of the airborne equipment is connected by a single wire. For this reason, the induced voltage or current of unshielded single wire under 50 ohm load and open circuit and short circuit is analyzed below. Tables 6, 7, and 8 are the induced voltage or current peak values under the condition of single-line 50 Ω load and open circuit and short circuit, respectively.

Comparing the current and voltage values of the same point on the single line and the coaxial line, it is found that no matter the single line or the coaxial line, the values are basically the same, and the shapes of each point are similar. But even at both ends of a wire, the peak current and voltage will not be exactly the same. Because the current flows from the nose to the tail of the machine, the current of the internal cable near the nose is always greater than that far from the nose, and so is the voltage. When the current decreases, due to the different external magnetic fields in different regions, the coupling effect on the cable is also different. There are

Table 6: Coupling current (A) and voltage (V) of terminal on single-wire 50 Ω cable.

Coupling current		Coupling voltage	
Ia	0.304	*Va*	15.26
Ib	1.998	*Vb*	99.82
Ic	4.9	*Vc*	244.007
Id	5.671	*Vd*	283.538

Table 7: Short-circuit current (A) at the terminal when a single wire is short-circuited.

Ia	*Ib*	*Ic*	*Id*
0.434	2.568	10.121	10.164

Table 8: Open-circuit voltage (V) at the terminal when single wire is open.

Va	*Vb*	*Vc*	*Vd*
490.901	530.285	1849	1765

also losses on the cable, which all lead to a reduction in current during transmission.

When a single wire is shorted or open, the current on the cable at the tail greatly varies because the current on the cable is mainly affected by the internal field. In the previous analysis, it can be seen that the field strength changes at the transponder, and the tail are still very large, so the current values at points *a* and *b* also change a lot. At point *b*, since point *b* is closer to the landing gear, the field strength is larger, so the current at *b* is greater than at a. However, both points *c* and *d* are in the cargo compartment, and the field strength does not change much, so the current difference is not large.

4. Conclusions

In order to analyze the lightning coupling of airborne secondary radar electronic equipment, based on the simulation calculation technology of the transmission-line matrix method, this study analyzes the transient electromagnetic field intensity of the airborne secondary radar electronic equipment and the current density distribution on the surface of the aircraft when the lightning directly hits the aircraft. On this basis, the simulation research of field distribution and cable coupling is further carried out. The simulation results are as follows:

(1) It can be seen from the simulation calculation that when the lightning strikes the aircraft, the current density at the continuum of the upper and lower surfaces of the fuselage and the middle of the wing is relatively small. In addition to the areas where the lightning current is easy to attach, structural irregularities such as windows, engines, front and rear edges of wings, and outboard antennas are often affected by edge effects, and the current density is often concentrated, requiring key protection.

(2) Inside the aircraft, the peak value of the electric field intensity near the transponder can reach 1.2 kV/m, and the peak value of the magnetic field can reach 36 A/m. In the vicinity of the electronic equipment at the belly, the peak value of the electric field strength can reach 8.3 kV/m, and the peak value of the magnetic field can reach 65 A/m. The main reason for the analysis is that the hole leakage caused by the hatch at the belly is the most serious. Therefore, the electronic equipment should be protected here, or the shielding effect of the hatch should be strengthened.

(3) For cables connected to electronic equipment, the open-circuit voltage can reach 1849 V, and the short-circuit current can reach 10 A. Since the current induced on a single line can reach about 200 times, the current is induced on a single-layer shielded line, that is, the shielding effectiveness of a single-layer shielded line is greater than about 45 dB. Therefore, for the more sensitive electronic equipment, the cable connected to it can be considered to use the appropriate type of shielded cable to achieve the shielding effect on the electromagnetic environment.

Data Availability

The data that support the findings of this study are available from the corresponding author upon reasonable request.

Conflicts of Interest

The authors declare that they have no conflicts of interest.

References

[1] X. Xiu, L. F. Luo, X. Fan, and L. Wang, "A review of the direct effects of aircraft lightning," *Aircraft Design*, vol. 21, no. 4, pp. 64–68, 2011.

[2] T. S. Wang, "Aircraft lightning protection," *Aircraft Design*, vol. 2001, no. 4, pp. 48–52+71, 2001.

[3] Y. Zhang, X. L. Si, Y. M. Li, S. S. Qiu, Z. B. Li, and Z. M. Duan, "Simulation research on lightning protection design of aircraft radar," *Journal of Hefei University of Technology*, vol. 42, no. 9, pp. 1222–1226+1291, 2019.

[4] Z. Y. Zhao and T. Yu, "Simulation on lightning damage to airborne secondary radar antenna," *Journal of Nanoelectronics and Optoelectronics*, vol. 14, no. 9, pp. 1290–1303, 2019.

[5] Y. Q. Huo, B. Wang, D. Gao, and C. Guo, "The damage and protection strategies of lightning inductance to electronic equipment on board," *Aeronautical Computing Technology*, vol. 39, no. 4, pp. 123–126, 2009.

[6] A. Ulmann, P. Brechet, A. B. Clergerie et al., "New investigations of the mechanisms of lightning strike to radomes Part I: experimental study in high voltage laboratory," *SAE Transactions*, vol. 110, pp. 325–331, 2001.

[7] Y. J. Li, P. F. Zhao, T. Wu, and Z. Y. Ding, "Analysis of aircraft lightning hazards and protection design," *Dual-use technology and products*, vol. 2019, no. 11, 55 pages, 2019.

[8] J. L. Huang, *Simulation and Research on Indirect Effects of Aircraft Lightning*, Southwest Jiaotong University, Sichuan, China, 2016.

[9] C. Chen, Y. Wei, Z. Yang, C. Enrong, and Z. Runqing Jiaming, "Simulation and analysis of EMP transient electromagnetic effect of aircraft," *Journal of Engineering*, vol. 2019, no. 16, pp. 2464–2467, 2019.

[10] T. Chen, S. S. Qiu, X. L. Si, Z. M. Duan, Z. B. Li, and Y. Li, "Simulation of lightning current distribution in the vertical tail of an airliner and lightning test research," *Fiber Composite Materials*, vol. 38, no. 3, pp. 12–17, 2021.

[11] G. S. Zhen, J. Z. Zang, and X. F. Qi, "Evaluation method of aircraft lightning current conduction path based on numerical simulation," *Advances in Aeronautical Engineering*, vol. 12, no. 1, pp. 136–142, December, 2012.

[12] C. Gao, S. Song, Y. C. Guo, and Q. Yang, "Simulation study on the division of aircraft lightning strike attachment area," *Journal of Radio Wave Science*, vol. 27, no. 6, pp. 1238–1243, 2012.

[13] L. Huang, C. Gao, F. Guo, and C. Sun, "Lightning indirect effects on helicopter: numerical simulation and experiment validation," *IEEE Transactions on Electromagnetic Compatibility*, vol. 59, no. 4, pp. 1171–1179, 2017.

[14] Z. Y. Zhao and Y. Z. Cui, "Simulation research on the influence of aircraft fuselage materials on the electromagnetic environment in the cabin," *Electric Porcelain Arrester*, vol. 2021, no. 4, 21 pages, 2021.

[15] J. X. Li, N. L. He, and Z. Y. Zhao, "Aziya. Analysis of lightning protection technology of aircraft weather radar radome," *Electronic Production*, vol. 2013, no. 21, 39 pages, 2013.

[16] J. Fang, D. W. Dai, and Z. J. Nie, "Research on the protection of indirect effects of lightning on special military aircraft," *Instrumentation Technology*, vol. 2018, no. 5, 49 pages, 2018.

[17] F. Guo, Z. L. Jiang, and L. Y. Su, "Simulation Analysis of the Indirect Effect Test Method of UAV Lightning [C]," in *Proceedings of the 35th Annual Meeting of the Chinese Meteorological Society S19 Lightning Physics and Lightning Protection New Technology - the 16th Session Thunder Disaster Reduction Forum*, pp. 100–102, Chicago, IL, USA, December 2018.

[18] Z. Y. Zhao, Z. S. Tang, and H. L. Huang, "Simulation of lightning electromagnetic environment in aircraft cabin," *Journal of Radio Wave Science*, vol. 30, no. 2, pp. 391–395, 2014.

[19] F. Guo, B. H. Zhou, and C. Gao, "Numerical simulation analysis of indirect effects of aircraft lightning," *Journal of Radio Wave Science*, vol. 27, no. 06, pp. 1129–1135, 2012.

[20] Z. M. Duan, "Overview of lightning protection for aircraft," *High Voltage Technology*, vol. 43, no. 5, pp. 1393–1399, 2017.

[21] M. Apra, M. D'Amore, K. Gigliotti, M. S. Sarto, and V. Volpi, "Lightning indirect effects certification of a transport aircraft by numerical simulation," *IEEE Transactions on Electromagnetic Compatibility*, vol. 50, no. 3, pp. 513–523, August, 2008.

[22] T. N. Zhao and S. K. Liu, "Test method for indirect effects of aircraft lightning," *Shanghai Metrology and Testing*, vol. 45, no. S1, pp. 6–10, 2018.